

# Numerical simulation of single droplet dynamics in three-phase flows using ISPH

Nima Tofighi, Mehmet Yildiz\*

Faculty of Engineering and Natural Sciences, Sabanci University, Tuzla, 34956, Istanbul, Turkey

---

## ARTICLE INFO

### Article history:

Received 14 December 2012

Received in revised form 14 April 2013

Accepted 21 May 2013

### Keywords:

Smoothed particle hydrodynamics (SPH)

Surface tension

Three-phase flow

## ABSTRACT

In this study, a new surface tension formulation for modeling incompressible, immiscible three-phase fluid flows in the context of incompressible smoothed particle hydrodynamics (ISPH) in two dimensions has been proposed. A continuum surface force model is employed to transform local surface tension force to a volumetric force while physical surface tension coefficients are expressed as the sum of phase specific surface tension coefficients, facilitating the implementation of the proposed method at triple junctions where all three phases are present. Smoothed color functions at fluid interfaces along with artificial particle displacement throughout the computational domain are combined to increase accuracy and robustness of the model. In order to illustrate the effectiveness of the proposed method, several numerical simulations have been carried out and results are compared to analytical data available in literature. Results obtained by simulations are compatible with analytical data, demonstrating that the ISPH scheme proposed here is capable of handling three-phase flows accurately.

---

## 1. Introduction

Multiphase flows where two or more fluids have interfacial contact surfaces are one of the most common features observed in many engineering and natural processes and have been a subject of interest for modeling in many computational fluid dynamics (CFD) studies. It is indeed a challenging problem as the evolution of the interface is a crucial step in modeling of multiphase flows which needs to be handled delicately to result in reliable simulations.

In their simplest form, multiphase flows are composed of two immiscible fluid streams. Many studies have been performed on two-phase flows using mesh dependent, meshless and hybrid approaches. Mesh dependent methods include Volume of Fluid (VOF) [1–3], Level Set (LS) [4–6] and Phase Field methods [7,8] where the interface is captured implicitly through use of a scalar function. These methods are also referred to as Eulerian approaches. Hybrid Eulerian–Lagrangian approaches, such as the Front Tracking method [9,10], provide a sharper interface representation by employing markers to track the interface explicitly, which adds to their accuracy at the cost of extra complexity and computational expense. In this regard, the Lagrangian nature of meshless methods is an inherent advantage of this kind of approach as it facilitates the tracking of interfaces with large deformations. Among all different variants of meshless methods, Smoothed Particle Hydrodynamics (SPH) has received a great deal of attention in modeling multiphase flows [11–18].

Despite the large pool of research available in two-phase flows, there have been relatively fewer studies carried out on flows containing three different fluids, partly due to complexities inherent in phase interactions and possible triple-junctions present in these flows. A few examples include level set studies of triple junctions [19,20] and droplet spreading [21],

---

\* Corresponding author. Tel.: +90 2164839517.

E-mail addresses: [meyildiz@sabanciuniv.edu](mailto:meyildiz@sabanciuniv.edu), [myildiz@uvic.ca](mailto:myildiz@uvic.ca) (M. Yildiz).

droplet impact simulation using front tracking [22], phase field simulations of several three-phase flows [23,24] and weakly compressible smoothed particle hydrodynamics simulations of two- and three-phase flows [25].

In this study, an incompressible SPH (ISPH) scheme based on the projection method initially proposed by Cummins and Rudman [26] is developed to simulate two-dimensional immiscible three-phase flows. Surface tension forces are taken into consideration using the Continuum Surface Force (CSF) model proposed by Brackbill et al. [27]. In order to capture the interaction between different phases, the surface tension coefficient decomposition method proposed in Smith et al. [20] has been employed. A number of test cases have been simulated to test the capabilities of the proposed scheme in a methodical manner. First, elongation of a circular droplet encompassed between two immiscible fluid layers have been studied and compared to analytic values. Extending this test case towards a more dynamic one, levitation of a circular droplet initially at rest between two layers of immiscible fluids have been simulated. Finally to demonstrate flexibility of the method in handling moving contact lines involving density and viscosity differences, simulations of droplet spreading on a solid surface are conveyed and compared against analytical results available in literature.

The outline of this paper is as follows. Mathematical formulation along with numerical approximations employed are presented in Sections 2 and 3. Results of the simulations and validations against literature data are presented and discussed in Section 4 and concluding remarks are drawn in Section 5.

## 2. Mathematical formulation

Mass and momentum conservation equations for an incompressible flow may be written as

$$\nabla \cdot \mathbf{u} = 0, \quad (1)$$

$$\rho \frac{D\mathbf{u}}{Dt} = -\nabla p + \nabla \cdot \boldsymbol{\tau} + \mathbf{f}_{(b)} + \mathbf{f}_{(s)}, \quad (2)$$

where  $\mathbf{u}$  is the velocity vector,  $p$  is pressure,  $\rho$  is density,  $t$  is time and  $D/Dt = \partial/\partial t + u^k \partial/\partial x^k$  represents the material time derivative. Here,  $\boldsymbol{\tau}$  and  $\mathbf{f}_{(b)}$  are viscous stress tensor and body forces exerted on the flow, respectively. While the body force is taken to be  $\rho \mathbf{g}$  where  $\mathbf{g}$  is gravitational acceleration, the viscous stress tensor is defined as

$$\boldsymbol{\tau} = \mu (\nabla \mathbf{u} + (\nabla \mathbf{u})^T), \quad (3)$$

where superscript  $T$  represents the transpose operation. For the sake of computational simplicity and efficiency, it is preferable to express the local surface force as an equivalent volumetric force,  $\mathbf{f}_{(s)}$ , according to the Continuum Surface Force (CSF) method originally proposed by Brackbill et al. [27]. Replacing the sharp interface between two fluids with a transitional region of finite thickness through multiplication of local surface tension force with a one-dimensional Dirac delta function [28],  $\delta$ , surface tension force may be formulated as

$$\mathbf{f}_{(s)} = \sigma \kappa \hat{\mathbf{n}} \delta. \quad (4)$$

Here, surface tension coefficient,  $\sigma$ , is taken to be constant while  $\kappa$  represents interface curvature,  $-\nabla \cdot \hat{\mathbf{n}}$ , where  $\hat{\mathbf{n}}$  is unit surface normal vector.

The above definition for volumetric surface tension force has to be developed further if it is to be used for a three-phase flow as a fluid particle may be affected by more than two interfaces simultaneously, which is the case near triple junctions where all three phases meet. In order to circumvent this difficulty, Smith et al. [20] have proposed decomposing the surface tension coefficient into phase specific surface tension coefficients such that  $\sigma^{\alpha\beta} = \sigma^\alpha + \sigma^\beta$ . Here,  $\sigma^{\alpha\beta}$  is the physical surface tension coefficient between phases  $\alpha$  and  $\beta$  while  $\sigma^\alpha$  and  $\sigma^\beta$  are phase specific surface tension coefficients for  $\alpha$ th and  $\beta$ th phases, respectively. Considering a three-phase flow, the aforementioned decomposition will lead to the following relations for phase specific surface tension coefficients,

$$\begin{cases} \sigma^1 = 0.5 (\sigma^{12} + \sigma^{13} - \sigma^{23}), \\ \sigma^2 = 0.5 (\sigma^{12} - \sigma^{13} + \sigma^{23}), \\ \sigma^3 = 0.5 (-\sigma^{12} + \sigma^{13} + \sigma^{23}). \end{cases} \quad (5)$$

Combining phase specific surface tension coefficients defined above with (4), the resultant volumetric surface tension force may be rewritten as a sum of three force components as

$$\mathbf{f}_{(s)} = \sum_{\alpha=1}^3 (\sigma \kappa \hat{\mathbf{n}} \delta)^\alpha. \quad (6)$$

To be able to distinguish different fluids of the three-phase flow of interest, three concurrent color functions are introduced where each one is associated to a certain phase. Thus the color function for phase  $\alpha$ ,  $\hat{c}^\alpha$ , has a value of one where phase  $\alpha$  is present while other color functions are set to zero. Interface curvature, unit normals and surface tension forces related to each phase are computed using its corresponding color function and will be discussed further in the following section.

### 3. Numerical scheme

Interactions between SPH particles are facilitated through the use of an interpolation kernel,  $W(r_{ij}, h)$ , concisely referred to as  $W_{ij}$  for a constant  $h$ . Here,  $r_{ij}$  is the magnitude of distance vector  $\mathbf{r}_{ij} = \mathbf{r}_i - \mathbf{r}_j$  between a particle of interest  $i$  and its neighboring particles  $j$  while  $h$  is referred to as the smoothing length which controls the interaction length among particles. Based on this smoothing kernel, the value of an arbitrary variable  $f$  in a two-dimensional domain  $\Omega$  over a set of discrete points may be written as  $f(\mathbf{r}) \simeq \int_{\Omega} f(\mathbf{r}_j) W_{ij} d\mathbf{r}_j^2$ . Replacing the integral operation with a summation operation over all the particles within a certain cut-off distance and approximating the infinitesimal volume element by the reciprocal of the number density  $\psi_j$ , defined for the particle  $j$ , one can write the SPH approximation as

$$f(\mathbf{r}) \simeq \sum_j \frac{1}{\psi_j} f_j W_{ij}, \quad (7)$$

where  $f_j$  denotes  $f(\mathbf{r}_j)$  and the number density for particle  $i$  is defined as  $\psi_i = \sum_j W_{ij}$ .

In order to be able to interpolate fluid properties across the interface properly and further enhance the robustness of the method, the color function for particle  $i$  of phase  $\alpha$ ,  $\hat{c}_i^\alpha$ , is smoothed as

$$c_i^\alpha = \frac{\sum_j \hat{c}_j^\alpha W_{ij}}{\psi_i}. \quad (8)$$

The smoothed color function thus acquired may be used to smoothen the sharp gradients in properties that may potentially destabilize the numerical method using a weighted averaging scheme over all phases,  $f_i = \sum_{\alpha=1}^3 f_i^\alpha c_i^\alpha$ . Here  $f$  may represent density or viscosity of the flow at particle  $i$  where appropriate. The smoothed color function is also used to define  $\delta^\alpha \simeq |\nabla c^\alpha|$ ,  $\kappa^\alpha = -\nabla \cdot \hat{\mathbf{n}}^\alpha$  and  $\hat{\mathbf{n}}^\alpha = \nabla c^\alpha / |\nabla c^\alpha|$  in (6) for each phase, combining which will result in the following relation for volumetric surface tension force,

$$\mathbf{f}_{(s)} = - \sum_{\alpha=1}^3 \sigma^\alpha \nabla \cdot \left( \frac{\nabla c^\alpha}{|\nabla c^\alpha|} \right) \nabla c^\alpha. \quad (9)$$

A constraint has to be enforced to keep possible erroneous normals that may occur at the outer edges of interface from contaminating the computed surface tension force, as pointed out by Morris [29]. In this study, only gradient values exceeding a certain threshold,  $|\nabla c_i| \simeq \varepsilon/h$ , are used in surface tension force calculations. An  $\varepsilon$  value of 0.08 has been found to provide accurate results without removing too much detail.

A predictor–correcter scheme is employed to advance the governing equations of flow in time using a first-order Euler approach with variable timestep according to the Courant–Friedrichs–Lewy condition,  $\Delta t = C_{CFL} h / u_{\max}$ , where  $u_{\max}$  is the largest particle velocity magnitude and  $C_{CFL}$  is taken to be equal to 0.25. In the predictor step all the variables are advanced to their intermediate form using following relations,

$$\mathbf{r}_i^* = \mathbf{r}_i^{(n)} + \mathbf{u}_i^{(n)} \Delta t + \delta \mathbf{r}_i^{(n)}, \quad (10)$$

$$\mathbf{u}_i^* = \mathbf{u}_i^{(n)} + (\nabla \cdot \boldsymbol{\tau}_i + \mathbf{f}_{(b)i} + \mathbf{f}_{(s)i})^{(n)} \Delta t, \quad (11)$$

$$\psi_i^* = \psi_i^{(n)} - \Delta t \psi_i^{(n)} (\nabla \cdot \mathbf{u}_i^*), \quad (12)$$

where starred variables represent intermediate values and the superscript  $(n)$  denotes values at the  $n$ th timestep. Following the SPH approximation in (7), the first order derivatives may be discretized as

$$\frac{\partial f_i^m}{\partial x_i^k} a_i^{kl} = \sum_j \frac{1}{\psi_j} (f_j^m - f_i^m) \frac{\partial W_{ij}}{\partial x_i^k}, \quad (13)$$

while the Laplace operator is approximated in the following manner,

$$\frac{\partial^2 f_i^m}{\partial x_i^k \partial x_i^k} a_i^{ml} = 8 \sum_j \frac{1}{\psi_j} (f_j^m - f_i^m) \frac{r_{ij}^m}{r_{ij}^2} \frac{\partial W_{ij}}{\partial x_i^l}. \quad (14)$$

Here,  $a_i^{kl} = \sum_j \frac{r_{ij}^k}{\psi_j} \frac{\partial W_{ij}}{\partial x_i^l}$  is a corrective second rank tensor that eliminates particle inconsistencies [30]. A cubic spline kernel [31] is employed for equations relevant to the surface tension force while a quintic spline kernel [32] is used for other cases. The same value of  $h$ , equal to 1.4 times the initial particle spacing, is used for both kernels and kept constant in the temporal and spatial directions during simulations. This practice facilitates a thinner interface and produces larger  $\delta^\alpha$

values which result in more accurate surface tension force calculations [28]. Defining average particle spacing for a given particle  $i$  having  $J$  neighbors as  $r_{av,i} = \sum_j (r_{ij}/J)$ , the artificial particle displacement vector in (10),  $\delta \mathbf{r}_i$ , is calculated as

$$\delta \mathbf{r}_i^{(n)} = \gamma \sum_{j=1}^J \left( \frac{\mathbf{r}_{ij}}{r_{ij}^2} r_{av,i}^2 u_{\max} \right)^{(n)} \Delta t. \quad (15)$$

A range of different values have been tested for the cases studied here and a value of  $\gamma = 0.06$  is found to have a satisfactory particle distribution and stabilizing effect [28], which is employed throughout this study.

Using intermediate values, pressure at the next timestep is found by solving the following Poisson equation,

$$\nabla \cdot \left( \frac{1}{\rho^*} \nabla p^{(n+1)} \right) = \frac{\nabla \cdot \mathbf{u}^*}{\Delta t}, \quad (16)$$

where the left hand side is approximated by

$$\frac{\partial^2 f_i^m}{\partial x_i^k \partial x_i^k} (2 + a_i^{kk}) = 8 \sum_j \frac{1}{\psi_j} (f_i^m - f_j^m) \frac{r_{ij}^k}{r_{ij}^2} \frac{\partial W_{ij}}{\partial x_i^k}, \quad (17)$$

which is then used to correct the velocity of the particles, hence advancing them to next timestep using the following relation,

$$\mathbf{u}^{(n+1)} = \mathbf{u}^* - \frac{1}{\rho} \nabla p^{(n+1)} \Delta t. \quad (18)$$

However, in order to be able to handle larger density ratios between different phases of the flow, an alternative form of (18) is considered here. By substituting  $\nabla p/\rho$  with its equivalent form,  $\nabla(p/\rho) - p\nabla(1/\rho)$ , the pressure correction term on the right hand side of (18) is discretized as

$$\begin{aligned} \frac{1}{\rho} \frac{\partial p_i}{\partial x_i^k} a_i^{kl} &= \left( \sum_j \frac{1}{\psi_j} \left[ \left( \frac{p_j}{\rho_j} - \frac{p_i}{\rho_i} \right) - \left( \frac{p_i}{\rho_j} - \frac{p_i}{\rho_i} \right) \right] \frac{\partial W_{ij}}{\partial x_i^l} \right) \\ &= \left( \sum_j \frac{1}{\rho_j \psi_j} (p_j - p_i) \frac{\partial W_{ij}}{\partial x_i^l} \right). \end{aligned} \quad (19)$$

This form, also referred to as the non-conservative form [33], ensures a zero pressure gradient when a particle of interest and its neighbors are of identical pressure. Having found velocity vector values at the next timestep, particles are moved to their corrected positions using the following relation,

$$\mathbf{r}_i^{(n+1)} = \mathbf{r}_i^{(n)} + \frac{1}{2} \left( \mathbf{u}_i^{(n)} + \mathbf{u}_i^{(n+1)} \right) \Delta t + \delta \mathbf{r}_i^{(n)}, \quad (20)$$

and number density values are restored to that of the previous timesteps.

Boundary conditions are test case dependent and are enforced through the MBT method described in [34].

## 4. Results

### 4.1. Liquid lens

In this section, simulation results for the liquid lens test case are presented and compared against analytical equilibrium lens diameter. Having an analytical solution, this test case is very well suited for testing the accuracy of the proposed scheme for modeling three-phase flows. The computational domain for every simulation is taken to be a square with a side length of  $l$ . Three different particle resolutions of  $R_1$ ,  $R_2$  and  $R_3$  have been used in simulations which have  $50 \times 50$ ,  $100 \times 100$  and  $200 \times 200$  particles, respectively. The initial particle arrangement scheme along with its relation to  $l$  will be elaborated further in the following paragraphs. All fluid properties are set to unity for every phase involved in simulations while binary surface tension coefficients assume different values depending on the test cases considered. Table 1 summarizes the important simulation parameters and results obtained for surface tension coefficient ratios of  $V_1$  through  $V_5$  at each of the resolutions  $R_1$ ,  $R_2$  and  $R_3$ . Different phases are ordered as shown in Fig. 1-b and d. No slip and zero pressure gradient boundary conditions are applied to all boundaries.

#### 4.1.1. Effect of initial particle arrangement

It is observed that the initial particle arrangement has a profound effect on results obtained from SPH simulations [35]. Two different approaches were used to arrange initial particle positions in the following simulations. The first approach,

**Table 1**

Simulation parameters and results for liquid lens elongation test case.

#	$\sigma^{13}/\sigma^{12}$ ( $\sigma^{13} = \sigma^{23}$ )	$d_a$			$d_o/d_a$	$d_f/d_a$		
		$R_1$	$R_2$	$R_3$		$R_1$	$R_2$	$R_3$
$V_1$	0.8	0.4771	0.4830	0.4601	0.6527	0.9687	0.9827	0.9939
$V_2$	0.9	0.4501	0.4556	0.4340	0.6919	0.9702	0.9827	0.9881
$V_3$	1.0	0.4313	0.4366	0.4159	0.7220	0.9684	0.9785	0.9856
$V_4$	1.1	0.4173	0.4224	0.4024	0.7463	0.9647	0.9783	0.9819
$V_5$	1.2	0.4064	0.4114	0.3919	0.7663	0.9602	0.9786	0.9865

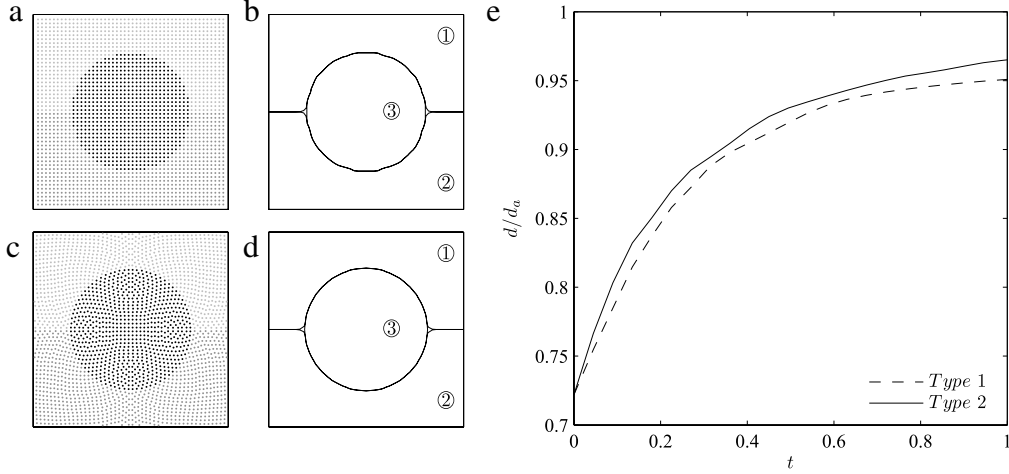


**Fig. 1.** Initial condition for liquid lens simulation shown in the vicinity of the droplet; (a, b) particle arrangement and 0.5 level contour of color function for the first approach. ①, ② and ③ denote phases 1, 2 and 3, respectively; (c, d) particle arrangement and 0.5 level contour of color function for the second approach; (e) early stage development of non-dimensional lens diameter for the first and second approach of initial particle arrangements.

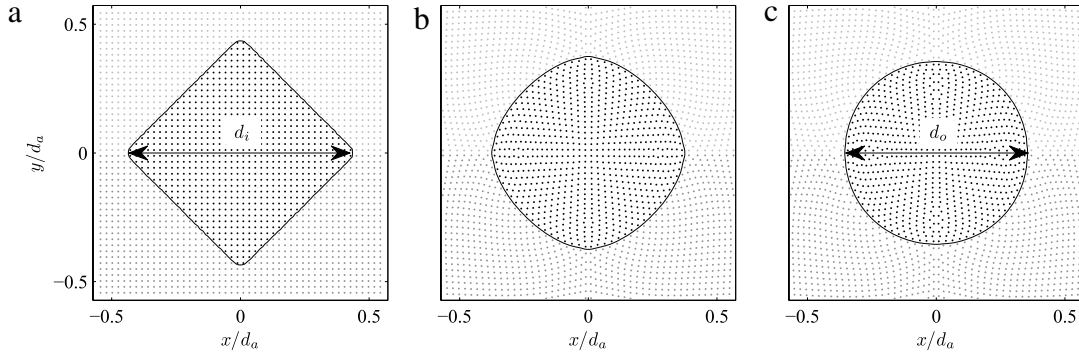


**Fig. 2.** Particle arrangement and 0.5 level contour of the color function for two-phase diamond relaxation; (a) initial diamond arrangement; (b) intermediate stage; (c) relaxed circle obtained and used as the initial particle arrangement for other test cases..

being the most straightforward one, consists of arranging the particles on an equally spaced formation in both dimensions. Particles within an “intended” radius of  $0.5d'_o$  from the center of computational domain are marked as phase 3 and are considered to belong to the droplet of interest, while the remaining particles are divided into top and bottom portions, phases 1 and 2 respectively (Fig. 1-a). This method results in a rough surface pattern with an approximate initial “acquired” diameter of  $d_o$  for the encompassed droplet.

The second method involves allowing a diamond ( $45^\circ$  tilted square) droplet of known area to deform into a circular droplet of an intended diameter of  $d'_o$  under the effect of surface tension forces in a two phase system, hence the two-phase diamond droplet relaxation shown in Fig. 2. To achieve this end within the scope of the proposed three-phase model, a particle arrangement with uniform spacing in both dimensions is used and particles within a diamond of the intended diagonal  $d'_i$  are considered as the droplet of interest, phase 3 (Fig. 2-a), while the remaining top and bottom portions are marked as phases 1 and 2, respectively. It is notable that due to finite spacing between particles, the acquired diagonal of the diamond is  $d_i$ , which is slightly smaller than  $d'_i$ . The computational domain length is chosen such that  $l = 2.6d'_i$  and the

diamond is relaxed in the two-phase mode by setting  $\sigma^{12} = 0$ . The resulting circular droplet has an acquired diameter of  $d_o$  and is used as an initial condition for particle arrangement (Figs. 1-c and 2-c).

In both cases, initial velocities are set to zero. These initial configurations are tested against analytical equilibrium lens diameter. Assuming that equilibrium contact angle is defined by

$$\frac{\sin \theta^1}{\sigma^{23}} = \frac{\sin \theta^2}{\sigma^{13}} = \frac{\sin \theta^3}{\sigma^{12}} \quad (21)$$

and  $\theta^1 = \theta^2$ , the equilibrium lens diameter is found using the following relation [24,36],

$$d_a = \left( \frac{2(\pi - \theta^1) - \sin(2(\pi - \theta^1))}{4A_o^2 \sin^2(\pi - \theta^1)} \right)^{-1/2}. \quad (22)$$

This defines the distance between two triple junctions and is based on Young's law where  $A_o$  represents initial droplet area and  $\theta^\alpha$  is the contact angle of phase  $\alpha$  with two other phases. Fig. 1-e shows non-dimensional lens diameter versus time at early stages of simulation for both initial conditions at resolution  $R_2$  where all binary surface tension coefficients are equal to 1. It is observable that the results obtained using the first initial condition type start to fall behind those of the second type at early stages of simulation. This trend continues at later simulation times yielding an equilibrium diameter,  $d_f/d_a$ , of 0.9519 for the first method against 0.9785 for the second method of initial condition generation. This is mainly due to the inaccurate measurement of the initial condition acquired diameter,  $d_o$ , in the first method of initial condition generation as well as the intermittent surface tension force observed when using a circular arrangement carved out of a Cartesian initial position. Therefore, all the simulation results presented hereafter are initialized using the second method.

#### 4.1.2. Effect of resolution and surface tension coefficient ratio

In this section, effects of resolution and surface tension coefficients on the evolution of the liquid lens are studied. It is worthwhile to note that different resolutions have different initial acquired diameter,  $d_o$ , because of the relaxation process involved in initial condition generation. It is not possible to create diamonds with the same acquired diagonal,  $d_i$ , using equally spaced particles at different resolutions for the same computational domain size as only multiples of the finite particle spacing are accessible. This results in different final acquired diameters,  $d_o$ , for initial diamond droplets of different resolution. However, once divided by the analytic equilibrium diameter, the resulting non-dimensional initial diameters will have the same value for each surface tension ratio group,  $V_1$  through  $V_5$ , which is shown in Table 1 as  $d_o/d_a$ . This ensures that when presented in non-dimensional form, the results will not be affected by the relaxation process.

Fig. 3-a shows near tip droplet profile for the three resolutions considered in this study while Fig. 3-b-d are non-dimensional lens diameter versus time plots for cases  $V_1$ ,  $V_3$  and  $V_5$ . It is observed that as the droplet lengthens under the effect of surface tension forces exerted, an equilibrium diameter is obtained. At this stage, the droplet starts to exhibit oscillations in diameter which is an expected behavior, providing that these oscillations will die out eventually. However, as the approximated differentiation and numerical implementation have small inherent round off errors affecting surface tension force which drives the lengthening phenomenon, the oscillations are not quite regular and are not damped out during the simulation times considered here. To circumvent this shortcoming, the lens diameter is time averaged after a certain threshold. Here, the averaging process starts as soon as the non-dimensional lens diameter reaches 95% of the analytic diameter. The time averaged equilibrium lens diameter is shown as a straight line for each resolution on Fig. 3-b-d and also in Table 1 under  $d_f/d_a$ . The result of this simple averaging criteria is not quite informative for cases with lower resolution as it disregards the transitional behavior and focuses on equilibrium diameter. This may result in over predicting the performance, as it is the case for  $R_1V_1$  where the time averaged equilibrium diameter is satisfactory despite an abnormally long transitional period. However, combining it with timed plots of non-dimensional diameter, which reveal irregular behavior such as slow lengthening observed in case  $R_1V_1$ , renders it a sufficient criteria for assessing the performance of the proposed method.

Comparing the time averaged values shown in Table 1, it is seen that better steady state results are obtained at higher resolutions. The effect of higher resolution is to make the triple junction slimmer, observable in Fig. 3-a as a sharper lens tip and a less abrupt cut, so that the remaining portion of the droplet has a smoother shape thus allowing it to extend furthermore towards the equilibrium diameter. Conducting a similar analysis on transient characteristics of the simulations (Fig. 3-b-d), it is possible to observe that the test case with lowest resolution,  $R_1$ , has the lowest rate of lengthening among all resolutions while higher resolutions considered here,  $R_2$  and  $R_3$ , exhibit the same characteristic initial lengthening rate. Slow lengthening is augmented for  $R_1$  cases as the final lens diameter becomes larger (more slender lens shape), which occurs as the ratio of surface tension coefficients,  $\sigma^{13}/\sigma^{12}$ , has a lower value. The reason for this effect may also be seen in Fig. 3-a. As the resolution is reduced, it is possible to identify an abrupt cut near the tip of the lens which affects the accuracy of the computed surface curvature and subsequently the surface tension force. At higher surface tension coefficient values, more slender equilibrium shapes occur which in turn should have sharper (smaller  $\theta^3$ ) three-phase junctions. This demands a higher resolution to be fully captured which results in a worse performance for the lower resolution test case and signifies the importance of higher resolution requirements for higher surface tension coefficient ratios.

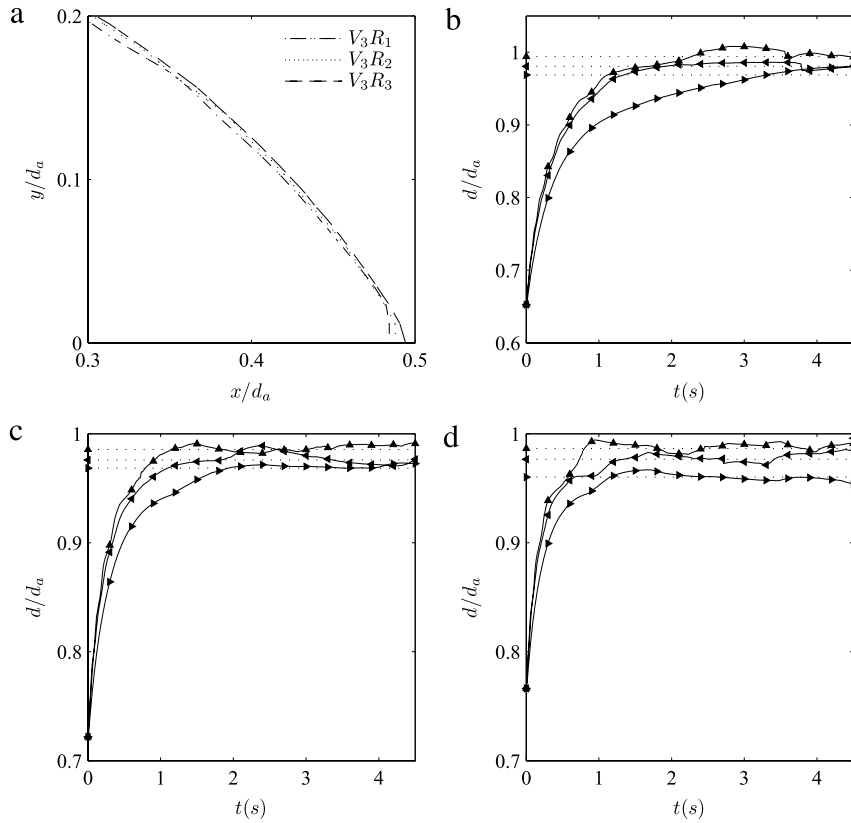


**Fig. 3.** (a) Effect of resolution on the equilibrium shape of test case  $V_3$  ( $V_3R_1$ ,  $V_3R_2$  and  $V_3R_3$ ); (b, c and d) effect of resolution on the equilibrium diameter of lens for cases  $V_1$ ,  $V_3$  and  $V_5$  where  $\blacktriangleright$ ,  $\blacktriangleleft$  and  $\blacktriangle$  denote  $R_1$ ,  $R_2$  and  $R_3$  resolutions, respectively. Straight lines and corresponding markers on vertical axis are time-averaged values,  $d_f/d_a$ , shown in Table 1.

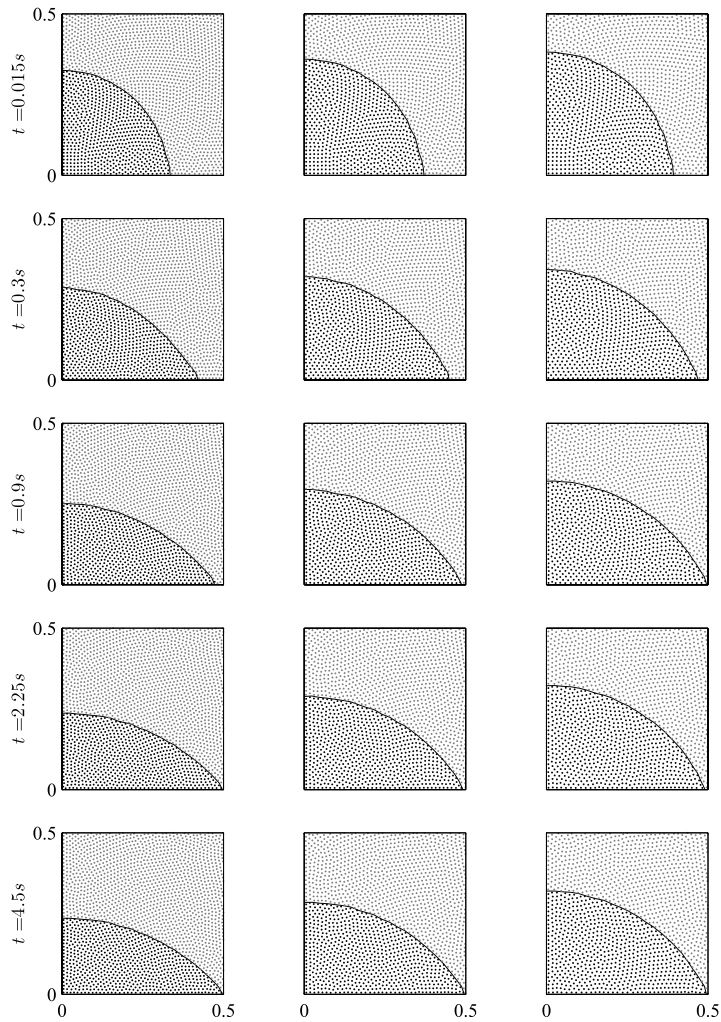
Fig. 4 shows time snapshots of the 0.5 level contour of the color function of the droplet, phase 3, along with particle positions for test cases  $V_1R_3$ ,  $V_3R_3$  and  $V_5R_3$ . As both dimensions are non-dimensionalized using analytic equilibrium lens diameter, the final length of the droplet will be equal to 0.5 while its height would be different. It is possible to observe that in all test cases shown, particles are spread fairly evenly across the computational domain, a desired property in SPH simulations which is a result of the artificial particle displacement method employed here.

Fig. 5 shows time snapshots of the 0.5 level of the color function contour at different time steps for all three phases of case  $V_3R_3$ . Each phase is actually treated as a separate entity when calculating surface tension forces using phase specific surface tension coefficients.

#### 4.2. Droplet levitation

In this section, results of the levitation of a circular droplet, initially at rest between two layers of immiscible fluids, are presented (Fig. 1-c and d). Droplet levitation presents a more challenging and dynamic problem to test the capabilities of the proposed three phase formulation as the droplet breaks free of the bottom surface and rises in top fluid solely because of surface tension forces as no other body forces are present. Here initial particle arrangement is obtained by relaxing a diamond shaped two-phase droplet consisting of  $200 \times 200$  particles into a circle of diameter  $d_o$ . Particle velocities in both directions are set to zero. All fluid properties except for surface tension coefficients are set to unity. As indicated in Table 2, surface tension coefficients between phases 1 and 2 ( $\sigma^{12}$ , top fluid and bottom fluid) and between phases 1 and 3 ( $\sigma^{13}$ , top fluid and droplet) are set to unity while the surface tension coefficient between the droplet and bottom fluid varies for different test cases. No slip and zero pressure gradient boundary conditions are applied to all the walls encompassing the computational domain, a square of  $3.3d_o$  side length.

Fig. 6 provides time snapshots of droplet levitation for all three test cases considered here. As the droplet starts to break off from the bottom surface, it experiences a deformation as a result of surface tension force exerted. The ratio of  $\sigma^{23}/\sigma^{13}$  has an important implication here as it directly influences the initial amount of the force exerted. This is better observable if average velocity,  $\mathbf{u}_{av} = \sum_{j=1}^J (\mathbf{u}_j/J)$ , of all particles belonging to phase 3,  $J$ , is investigated. Fig. 7 shows average vertical velocity,  $u_{av,y}$ , of the droplet for all the test cases. Times when snapshots in Fig. 6 have been taken are marked on Fig. 7 by identical letters. It is evident that larger surface tension ratios give rise to larger initial vertical velocity values. Table 2



**Fig. 4.** Time snapshots of particle position and droplet boundary (0.5 level contour of color function for droplet, phase 3). Both  $x$  and  $y$  axes are non-dimensionalized with each test case's respective analytic equilibrium diameter. Only the top right quarter has been shown for brevity. Left column: case  $V_1R_3$ ; middle column: case  $V_3R_3$ ; right column: case  $V_5R_3$ .

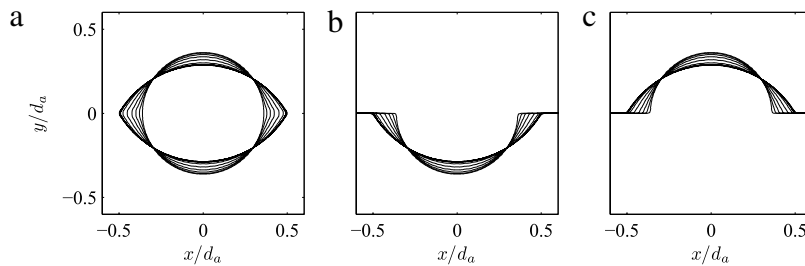


**Fig. 5.** Time snapshots of all phase boundaries (0.5 level contour of color function of each phase) for case  $R_3V_3$ . Both  $x$  and  $y$  axes are non-dimensionalized with respective analytic equilibrium diameter. (a) Droplet, phase 3; (b) bottom fluid, phase 2; (c) top fluid, phase 1.

summarizes maximum average vertical velocity for all cases studied here. Another impact of larger  $\sigma^{23}/\sigma^{13}$  is smaller  $\theta^1$  (angle between the droplet and bottom fluid) at the time when the droplet barely touches the bottom fluid. After separation is completed and the droplet is free of the bottom fluid, the droplet and top fluid pair are expected to act as a two-phase flow. This would result in a circular shape for the droplet after it comes to rest. All test cases studied here comply with this expectation although minor penetrations happen at the trailing edge of the droplet as it separates from the bottom fluid. The position where the droplet comes to rest is also affected by the value of  $\sigma^{23}/\sigma^{13}$ . Larger values result in a higher final position for the droplet.

**Table 2**  
Simulation parameters and results for the droplet levitation test case.

Test case	$\sigma^{23}/\sigma^{13}$ ( $\sigma_{12} = \sigma_{13}$ )	Maximum $u_{av,y}$
$L_1$	2.5	0.1730
$L_2$	5	0.4186
$L_3$	10	0.8541

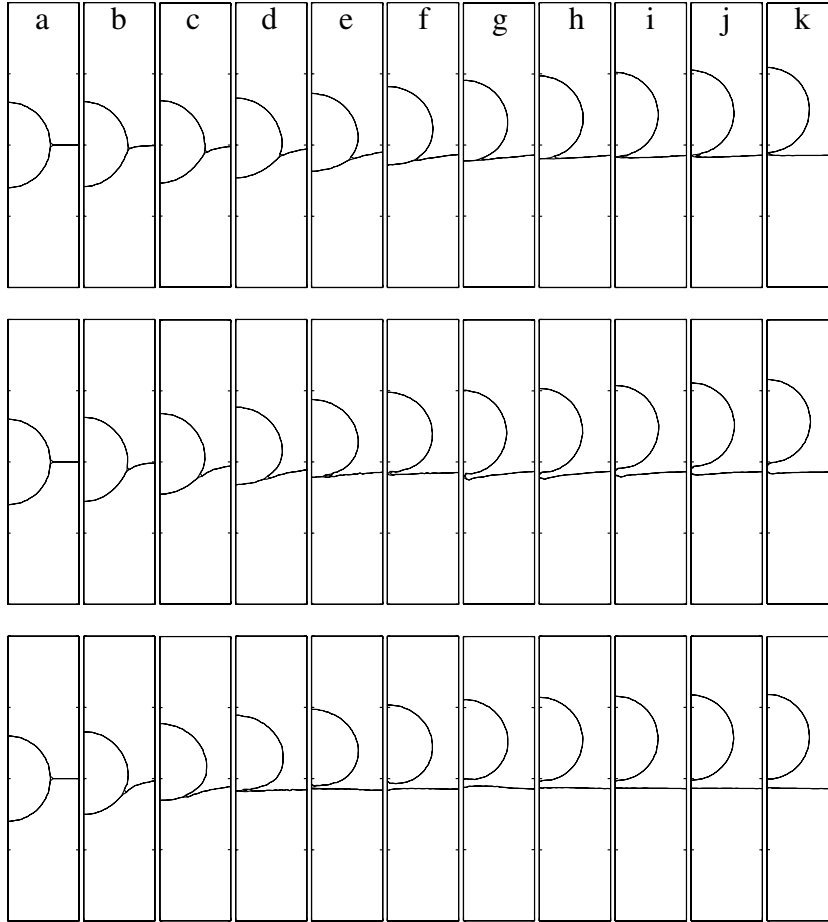


**Fig. 6.** Time snapshots of 0.5 level contour for all phases. Top row: case  $L_1$ ; middle row: case  $L_2$ ; bottom row: case  $L_3$ ; column letters  $a$  through  $k$  are at times 0, 0.03, 0.075, 0.15, 0.3, 0.6, 1.05, 1.5, 2.25, 3.0 and 4.5 s. Both  $x$  and  $y$  axes are non-dimensional with respect to  $d_0$  and tick marks are spaced 0.82 units apart.

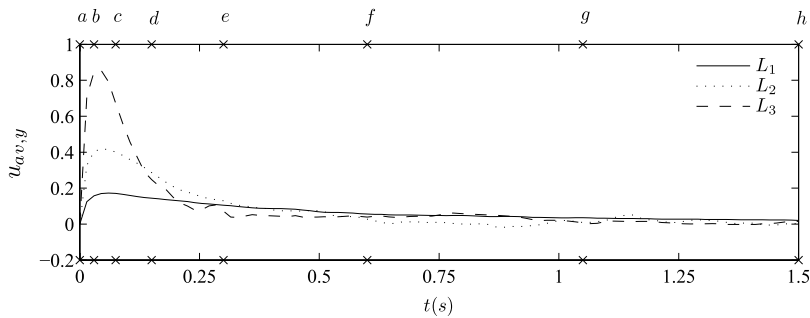


**Fig. 7.** Average vertical velocity of particles in droplet phase versus time for test cases  $L_1$ ,  $L_2$  and  $L_3$ . Letters and  $\times$  marks on horizontal axes represent the times when snapshots  $a$  through  $h$  in Fig. 6 are taken.

### 4.3. Droplet spreading

In order to demonstrate the capability of the proposed interface treatment scheme in handling moving contact line problems, droplet spreading simulations involving different Eotvos numbers are conveyed and results are compared to analytical solutions. The problem of interest is treated as a three-phase system where each of the fluid and solid phases have a distinct smoothed color function,  $c^\alpha$ , associated with them. Here, phases 1, 2 and 3 indicate surrounding fluid, droplet and solid bottom surface, respectively. A half circle droplet having a radius of  $R_0$  is positioned on the bottom surface centered at the origin. The computational domain has a non-dimensional size of  $3 \times 10$  and is discretized by  $60 \times 200$  of equally spaced particles in a Cartesian initial positioning. In addition to the particles within the computational domain, four rows of immovable particles are also appended to phase 3. These particles are lined up below the solid surface boundary with the same spacing as of the particles above the boundary. The motivation behind using this method is to have an accurate value for the smoothed color function,  $c^\alpha$ , unit normal,  $\hat{\mathbf{n}}^\alpha$ , and curvature,  $\kappa^\alpha$ . These particles are neither included in the calculation of other field variables nor in maintaining boundary conditions on the bottom surface.

Initially, all particles are assumed to be motionless. No slip and zero pressure gradient boundary conditions are enforced on all bounding walls, however, in order to circumvent shear stress singularity arising near contact line, no slip condition is relaxed to a local free slip at the vicinity of triple junction. Hence horizontal velocity is found using  $u_x = \lambda (\partial u_x / \partial y)_{wall}$ , where slip length,  $\lambda$ , is assumed to be infinite for particles having non zero  $c^\alpha$  for all phases. Accounting for the interface thickness, at most four boundary particles in the vicinity of the contact line are subject to this condition.

Under the combined effects of surface tension and gravitational forces, the droplet deforms until reaching its equilibrium shape. The steady state shape obtained by the droplet is dependent on the equilibrium contact angle,  $\theta_e$ , and Eotvos number,  $Eo = (\rho^2 - \rho^1) g R_0^2 / \sigma^{12}$ , where  $\rho^1$  and  $\rho^2$  are densities of droplet and surrounding fluid, respectively, and  $g$  is the gravitational acceleration acting downward. In all cases,  $\rho^2 / \rho^1$  is assumed to be equal to 20. Contact angle between droplet and solid surface is determined by the equilibrium of surface tension forces on the triple junction as indicated by (classical argument by Young,)  $\sigma^{23} + \sigma^{12} \cos \theta_e - \sigma^{13} = 0$ , which upon incorporating the definition of phase specific surface tension coefficients (5) may be rewritten as

$$\theta_e = \cos^{-1} \left( \frac{\sigma^1 - \sigma^2}{\sigma^1 + \sigma^2} \right). \quad (23)$$

In all test cases considered here,  $\sigma^1$  is set equal to  $\sigma^2$ , resulting in an equilibrium angle of  $90^\circ$ .

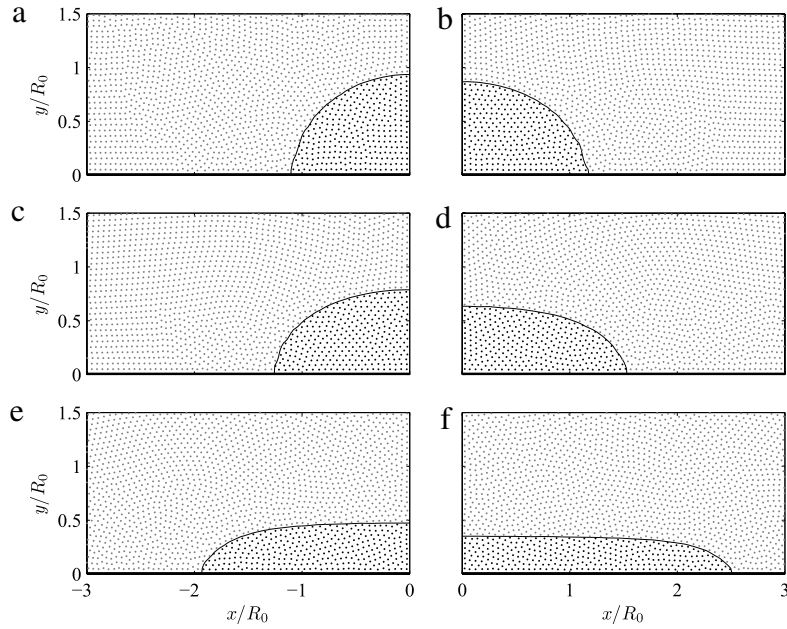
A high  $Eo$  (i.e.  $Eo \gg 1$ ) implies that the droplet shape is governed by gravitational forces whereas a low  $Eo$  (i.e.  $Eo \ll 1$ ) indicates a surface tension dominated shape at the steady state. Flows with intermediate values of  $Eo$  feature a non-trivial competition between these two effects. For  $Eo \gg 1$ , the analytical solution for the maximum height of the droplet is given by  $H = R_0 (1 - \cos \theta_e) \sqrt{\pi (2\theta_e - 2 \cos \theta_e \sin \theta_e)}$ . As for  $Eo \ll 1$ , the analytical solution indicates that the maximum height of the deformed droplet is proportional to  $Eo$  as  $H = 2R_0 Eo^{-1/2} \sin(\theta_e/2)$ . A set of simulations for  $0.1 \leq Eo \leq 13.3$  are performed and the results are compared with the aforementioned asymptotic analytical solutions.

Fig. 8 provides plots of the 0.5 level contour of the color function as well as particle placements at equilibrium for different  $Eo$  while Fig. 9 provides normalized steady state droplet height for  $0.1 \leq Eo \leq 13.3$ . As the difference between the initial and final shapes of the droplet for case  $Eo = 0.1$  is negligible, its contour plot is not shown here. It is observable that the computed normalized droplet height agrees well with the asymptotic solutions given for  $Eo \gg 1$  and  $Eo \ll 1$ . As for the intermediate values of  $Eo$ , a transition between spherical cap and puddle shape occurs. At higher  $Eo$ , the difference between the asymptotic solution and numerical results decreases.

## 5. Conclusion

In this study, a two-dimensional ISPH method for modeling incompressible, immiscible three-phase fluid flows has been developed. Surface tension coefficients are decomposed into phase specific coefficients and surface tension force is exerted by implementing the CSF model. To complement this, a unique color function is associated with each phase and then smoothed out to improve the robustness of the method while a threshold has been implemented for choosing reliable normals to increase the accuracy of computed surface tension force. Furthermore, artificial particle displacement has been employed to ensure uniform spread of particles throughout the computational domain. Several test cases have been simulated to ensure the capability of the method in handling various three-phase flow combinations.

Having an analytical solution, formation of a lens shape from a circular droplet under surface tension forces has been studied to facilitate testing the accuracy of the proposed method. Results show that this test case is highly sensitive to initial particle positioning, favoring an arrangement obtained from two-phase diamond droplet relaxation over a droplet simply carved out of an equally spaced particle arrangement. Simulations have been carried out in three different resolutions, revealing that an abrupt cut at the tip of the lens is responsible for the inaccuracies incurred at low resolutions. The results obtained from high resolution simulations at different surface tension ratios using improved initial conditions are found to be compatible with analytical solution of the equilibrium lens length. To further test the capabilities of the proposed method in handling dynamic problems, a droplet levitation test case has been simulated for different surface tension ratios. It is observed that, higher surface tension ratios result in faster break up from the surface due to a larger force exerted at the



**Fig. 8.** Equilibrium particle position and droplet boundary (0.5 level contour of color function, phase 2). Only half of the computational domain has been shown for brevity. Solid lines indicate bottom wall (phase 3). (a)  $Eo = 0.475$ ; (b)  $Eo = 0.95$ ; (c)  $Eo = 1.9$ ; (d)  $Eo = 3.8$ ; (e)  $Eo = 7.6$ ; (f)  $Eo = 13.3$ .

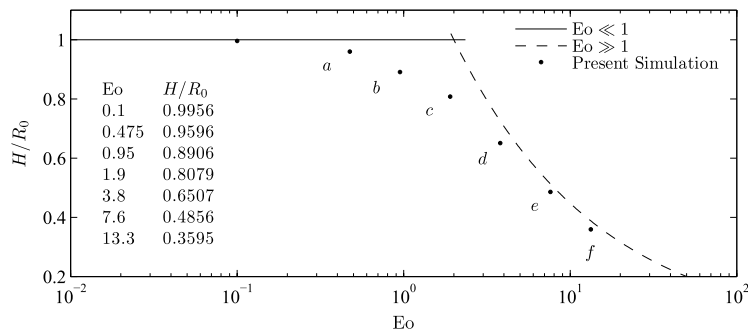


**Fig. 9.** Normalized equilibrium droplet height versus  $Eo$ . Letters *a* through *f* correspond to the droplet shapes shown in Fig. 8.

triple junction. Furthermore, a higher surface tension ratio resulted in larger maximum droplet velocity and higher stopping height. As the last test case, droplet spreading with a contact angle of  $90^\circ$  has been considered. With minor modifications, the method has been able to simulate contact line dynamics for a variety of Eotvos numbers, demonstrating the flexibility of the method and its capability in handling density and viscosity differences between phases. Results obtained for  $Eo \gg 1$  and  $Eo \ll 1$  are compatible with analytical values available for these two extremes while a transition from spherical cap to puddle shape occurs for  $Eo$  values in between.

The simulations conducted here and comparison of the results show that the proposed ISPH method is capable of handling different three-phase flow problems involving a single droplet.

## Acknowledgments

The authors gratefully acknowledge financial support provided by the Scientific and Technological Research Council of Turkey (TUBITAK) for the project 110M547 and the European Commission Research Directorate General under Marie Curie International Reintegration Grant program with the grant agreement number of PIRG03-GA-2008-231048.

## References

- [1] C.W. Hirt, B.D. Nichols, Volume of fluid (VOF) method for the dynamics of free boundaries, *J. Comput. Phys.* 39 (1981) 201–225.
- [2] D. Gueyffier, J. Li, A. Nadim, R. Scardovelli, S. Zaleski, Volume-of-fluid interface tracking with smoothed surface stress methods for three-dimensional flows, *J. Comput. Phys.* 152 (1999) 423–456.
- [3] D. Gao, N.B. Morley, V. Dhir, Numerical simulation of wavy falling film flow using VOF method, *J. Comput. Phys.* 192 (2003) 624–642.

- [4] M. Sussman, A.S. Almgren, J.B. Bell, P. Colella, L.H. Howell, M.L. Welcome, An adaptive level set approach for incompressible two-phase flows, *J. Comput. Phys.* 148 (1999) 81–124.
- [5] S. Osher, J.A. Sethian, Fronts propagating with curvature-dependent speed—algorithms based on Hamilton–Jacobi formulations, *J. Comput. Phys.* 79 (1988) 12–49.
- [6] J.A. Sethian, P. Smereka, Level set methods for fluid interfaces, *Annu. Rev. Fluid Mech.* 35 (2003) 341–372.
- [7] R. Chella, J. Vinals, Mixing of a two-phase fluid by cavity flow, *Phys. Rev. E* 53 (1996) 3832–3840.
- [8] V.E. Badalassi, H.D. Cenicerros, S. Banerjee, Computation of multiphase systems with phase field models, *J. Comput. Phys.* 190 (2003) 371–397.
- [9] S.O. Unverdi, G. Tryggvason, A front-tracking method for viscous, incompressible, multi-fluid flows, *J. Comput. Phys.* 100 (1992) 25–37.
- [10] G. Tryggvason, B. Bunner, A. Esmarelli, D. Juric, N. Al-Rawahi, W. Tauber, J. Han, S. Nas, Y.J. Jan, A front-tracking method for the computations of multiphase flow, *J. Comput. Phys.* 169 (2001) 708–759.
- [11] J.J. Monaghan, Simulating free-surface flows with SPH, *J. Comput. Phys.* 110 (1994) 399–406.
- [12] J.J. Monaghan, A. Kocharyan, SPH simulation of multiphase flow, *Comput. Phys. Comm.* 87 (1995) 225–235.
- [13] J.J. Monaghan, R.A.F. Cas, A.M. Kos, M. Hallworth, Gravity currents descending a ramp in a stratified tank, *J. Fluid Mech.* 379 (1999) 39–70.
- [14] M. Landrini, A. Colagrossi, M. Greco, M.P. Tulin, Gridless simulations of splashing processes and near-shore bore propagation, *J. Fluid Mech.* 591 (2007) 183–213.
- [15] N. Grenier, M. Antuono, A. Colagrossi, D. Le Touze, B. Alessandrini, An Hamiltonian interface SPH formulation for multi-fluid and free surface flows, *J. Comput. Phys.* 228 (2009) 8380–8393.
- [16] A. Ferrari, L. Fraccarollo, M. Dumbser, E.F. Toro, A. Armanini, Three-dimensional flow evolution after a dam break, *J. Fluid Mech.* 663 (2010) 456–477.
- [17] X. Xu, J. Ouyang, T. Jiang, Q. Li, Numerical simulation of 3D-unsteady viscoelastic free surface flows by improved smoothed particle hydrodynamics method, *J. Non-Newton. Fluid Mech.* 177 (2012) 109–120.
- [18] K. Szewc, J. Pozorski, J.P. Minier, Simulations of single bubbles rising through viscous liquids using smoothed particle hydrodynamics, *Int. J. Multiph. Flow* 50 (2013) 98–105.
- [19] B. Merriman, J.K. Bence, S.J. Osher, Motion of multiple junctions—a level set approach, *J. Comput. Phys.* 112 (1994) 334–363.
- [20] K.A. Smith, F.J. Solis, D.L. Chopp, A projection method for motion of triple junctions by level sets, *Interfaces Free Bound.* 4 (2002) 263–276.
- [21] M. Zhang, Simulation of surface tension in 2D and 3D with smoothed particle hydrodynamics method, *J. Comput. Phys.* 229 (2010) 7238–7259.
- [22] M. Muradoglu, S. Tasoglu, A front-tracking method for computational modeling of impact and spreading of viscous droplets on solid walls, *Comput. Fluids* 39 (2010) 615–625.
- [23] F. Boyer, C. Lapuerta, Study of a three component Cahn–Hilliard flow model, *ESAIM Math. Model. Numer. Anal.* 40 (2006) 653–687.
- [24] J. Kim, Phase field computations for ternary fluid flows, *Comput. Methods Appl. Mech. Eng.* 196 (2007) 4779–4788.
- [25] X.Y. Hu, N.A. Adams, A multi-phase SPH method for macroscopic and mesoscopic flows, *J. Comput. Phys.* 213 (2006) 844–861.
- [26] S.J. Cummins, M. Rudman, An SPH projection method, *J. Comput. Phys.* 152 (1999) 584–607.
- [27] J.U. Brackbill, D.B. Kothe, C. Zemach, A continuum method for modeling surface-tension, *J. Comput. Phys.* 100 (1992) 335–354.
- [28] A. Zainali, N. Tofighi, M.S. Shadloo, M. Yildiz, Numerical investigation of Newtonian and non-Newtonian multiphase flows using ISPH method, *Comput. Methods Appl. Mech. Engrg.* 254 (2013) 99–113.
- [29] J.P. Morris, Simulating surface tension with smoothed particle hydrodynamics, *Internat. J. Numer. Methods Fluids* 33 (2000) 333–353.
- [30] M.S. Shadloo, A. Zainali, S.H. Sadek, M. Yildiz, Improved incompressible smoothed particle hydrodynamics method for simulating flow around bluff bodies, *Comput. Methods Appl. Mech. Eng.* 200 (2011) 1008–1020.
- [31] J.P. Morris, A study of the stability properties of smooth particle hydrodynamics, *Publ. Astron. Soc. Aust.* 13 (1996) 97–102. Workshop on Magnetic Fields, Disks and Jets, Canberra, Australia, Apr 18–19, 1994.
- [32] J.J. Monaghan, J.C. Lattanzio, A refined particle method for astrophysical problems, *Astron. Astrophys.* 149 (1985) 135–143.
- [33] S.M. Hosseini, J.J. Feng, Pressure boundary conditions for computing incompressible flows with SPH, *J. Comput. Phys.* 230 (2011) 7473–7487.
- [34] M. Yildiz, R.A. Rook, A. Suleman, SPH with the multiple boundary tangent method, *Int. J. Numer. Methods Eng.* 77 (2009) 1416–1438.
- [35] A. Colagrossi, B. Bouscasse, M. Antuono, S. Marrone, Particle packing algorithm for SPH schemes, *Comput. Phys. Commun.* 183 (2012) 1641–1653.
- [36] J. Kim, Phase-field models for multi-component fluid flows, *Commun. Comput. Phys.* 12 (2012) 613–661.